BNL-223432-2022-JAAM

# Formation of a Secondary Phase in Thermally Evaporated MAPbI3 and Its Effects on Solar Cell Performance

A. Castro-Mendez, R. Li

To be published in "ACS Applied Materials and Interfaces"

May 2022

Photon Sciences

**Brookhaven National Laboratory**

**U.S. Department of Energy**

USDOE Office of Science (SC), Basic Energy Sciences (BES) (SC-22)

# DISCLAIMER

**Formation of a secondary phase in thermally evaporated $MAPbI_3$ and its effects on solar cell performance**

Andrés-Felipe Castro-Méndez[1], Carlo Andrea Riccardo Perini[1], Juanita Hidalgo[1], Daniel Ranke[1], Jacob N. Vagott[1], Yu An[1], Barry Lai[2], Yanqi Luo[2], Ruipeng Li[3], Juan-Pablo Correa-Baena[1*]

[1]School of Materials Science and Engineering, Georgia Institute of Technology, North Ave NW, Atlanta, Georgia 30332, USA

[2]Advanced Photon Source, Argonne National Laboratory, 9700 Cass Avenue, Lemont, Illinois 60439, United States

[3]National Synchrotron Light Source II, Brookhaven National Lab, Upton, New York 11973, USA

*Corresponding author: Juan-Pablo Correa-Baena, jpcorrea@gatech.edu

**Abstract**

Thermal evaporation is a promising deposition technique to scale up perovskite solar cells (PSCs) to large areas, but the lack of understanding on the mechanisms that lead to high quality evaporated methylammonium lead triiodide ($MAPbI_3$) films gives rise to devices with lower efficiencies than those obtained by spin coating. This work investigates the crystalline properties of $MAPbI_3$ deposited by thermal co-evaporation of $PbI_2$ and MAI, where the MAI evaporation rate is controlled by setting different temperatures for the MAI source, and the $PbI_2$ deposition rate is controlled with a quartz crystal microbalance (QCM). Using grazing incident wide-angle X-ray scattering (GIWAXS) and X-ray diffraction (XRD), we identify the formation of a secondary orthorhombic phase (with a Pnma space group) that appears at MAI source temperatures below 155 °C. With synchrotron-based X-ray fluorescence (XRF) microscopy, we show that the changes in crystalline phases are not necessarily due to changes in stoichiometry. The films show stochiometric composition when the MAI source is heated between 140 °C to 155 °C, and the samples become slightly MAI rich at 165 °C. Increasing the MAI temperature beyond 165 °C introduces an excess of MAI in the film, which promotes the formation of films with low crystallinity that contain low dimensional perovskites. Incorporated into solar cells, the films deposited at 165 °C result in the champion power conversion efficiency, although the presence of a small amount of low dimensional perovskite may lead to a lower open-circuit voltage. We hypothesize that the formation of secondary phases in evaporated films is limiting the performance of PSCs, and that their formation can be suppressed by controlling the MAI source temperature bringing the film towards a phase pure tetragonal structure. Control of the phases during perovskite evaporation is therefore crucial to obtain high performance solar cells.

**Keywords:** Perovskite Solar cells, thermal evaporation, thin films, crystalline phases, x-ray diffraction, x-ray fluorescence, methylammonium lead triiodide

## Introduction

In the face of growing demand for solar power, metal-halide perovskite solar cells (PSCs) have shown enormous potential as a low-cost photovoltaic technology. Since their inception in 2009, PSCs have seen an improvement in power conversion efficiency (PCE) from 3.8% [1] to over 25% on a lab-scale [2], surpassing the performance of polycrystalline silicon solar cells. However, to date, the most efficient PSCs are fabricated via solution processes hard to scale, such as spin-coating, posing concerns for the commercialization of this technology [3–6]. While spin-coating provides advantages during lab-scale fabrication for its low infrastructure cost, it lacks control over the film uniformity, stoichiometry, and morphology [7]. Moreover, the use of toxic organic solvents/antisolvents at the industrial level poses serious concerns for both hazard and handling costs [8]. Solvent-free perovskite deposition by means of thermal co-evaporation provides a facile methodology to enable more precise control over the environment and growth rate of perovskite films, and to produce high-quality, pinhole-free layers with great thickness control. Considering these advantages, devices fabricated with evaporated perovskites promise enormous potential to be scaled up for industrial operations. However, the PCEs of PSCs comprising vapor deposited active layers remain below 21% [9–13], lagging their solution-processed counterparts that now reach 25.7%[14–16]. Such difference is to be attributed to the lack of understanding of perovskite film formation via vapor, which limits the control on the optoelectronic properties of the deposited layer. In addition, the deposition rates of organic precursors of metal-halide perovskites such as methylammonium iodide (MAI), are difficult to control with quartz crystal microbalances (QCMs) [17].

For the deposition of the widely-studied methylammonium lead triiodide ($MAPbI_3$), MAI is evaporated alongside lead iodide ($PbI_2$) to form a homogeneous morphology of the crystalline film [18–21]. Experimentally, the MAI volatility and poor sticking factor at ambient temperatures complicate the measurement of the deposition rate of this organic salt with traditional QCMs [17], and can result in the formation of films with unreacted lead iodide [22]. Although a low level of excess $PbI_2$ in $MAPbI_3$ perovskites has been shown to boost device performance [23–26], too much unconverted $PbI_2$ can create an interfacial layer at the base of the perovskite film that hinders carrier transport across interfaces [22,27].

Much research has been devoted to controlling the rate of MAI deposition based on its partial pressure in the vacuum chamber and substrate temperature [28–30], allowing for the deposition of stoichiometrically-tuned films. However, the optimal deposition conditions do not easily extrapolate from laboratory to laboratory since they depend on system parameters such as pumping speed, volume of the chamber, temperature of the walls, and others. Moreover, the growth of co-evaporated perovskite films is still not fully understood, which results in lower efficiencies for vapor-deposited solar cells compared to state-of-the-art solution-processed devices.

Depositing $PbI_2$ at different deposition rates – with source temperatures ranging from room temperature to 320 °C - has a negligible effect on the total pressure in the chamber. On the other hand, the pressure increases up to two orders of magnitude when heating the MAI source, and it remains at a constant level once the temperature is set. As such, the MAI source temperature can be used as a parameter to control the deposition of MAI in the films in the same way that others have used chamber pressure to control the amount of evaporated MAI [29,30]. Differently from $PbI_2$, MAI has a low sticking factor and does not stick to the evaporator walls. As a result, MAI vapors fill the whole chamber volume and are present long enough to increase the pressure [31]. Figure S1 shows more information on the effect of temperature on the pressure of our system.

In this work, we show how the MAI source temperature - and thus the evaporation rate of MAI molecules – impacts the crystal structure, stoichiometry, and photovoltaic performance of the perovskite layer. We use a constant $PbI_2$ evaporation rate and different temperatures of the MAI source to induce the formation of films with different stoichiometries, whose crystalline properties we then analyze combining

X-ray Diffraction (XRD) and grazing-incidence wide-angle X-ray scattering (GIWAXS). Our results show that the use of different MAI evaporation rates has a strong impact – beyond stoichiometry - on the crystallinity of the deposited perovskite film and on its phase purity. Lower temperatures of MAI favor the formation of a secondary phase of $MAPbI_3$ that fits the Pnma space group, whereas higher temperatures result in the formation of LDP as consequence of higher incorporation of MAI in the film. If the temperature of the MAI source is raised beyond (e.g., 170 °C), the deposited layer becomes amorphous and strongly non-stoichiometric. The tetragonal perovskite phase is associated with higher PCEs, whereas mixed phases result in a performance drop.

**Experimental procedure**

$MAPbI_3$ was deposited in a commercial vacuum chamber (KJLC Minispectros) using two thermal sources equipped with alumina crucibles of 10 $cm^3$. One of the sources evaporates $PbI_2$ (Sigma Aldrich, 99%), while the other evaporates MAI (Great Solar, 99.99%). For $PbI_2$, the deposition rate was controlled using a QCM placed near the crucible, and the rate was fixed at 0.2 Å/s (unless specified otherwise). For MAI, the evaporation rate was controlled exclusively by selecting different fixed temperatures for the source. The MAI source temperature was varied from 80 °C to 170 °C to tune the final stoichiometry of the deposited perovskite film. A second QCM placed near the substrate monitored the thickness of the perovskite film deposited on the substrate. We calibrated both QCMs by measuring the layer thicknesses by profilometry prior to the experiments and found a good correlation between measured and actual thicknesses of the films. All the perovskite layers in this study have a thickness of 300 nm.

Our $MAPbI_3$ deposition process has three stages, as shown in Figure 1. In the first stage, we set the temperature of both sources right below the start temperature for evaporation of $PbI_2$ and MAI. These temperatures were kept constant for about 60 minutes. The purpose of this is to assure homogeneity between different runs since we observed an initial increase in the pressure that, thereafter, stabilizes at a lower value. Following this step, we increased the temperature of both sources and opened their respective shutters. The temperature of the MAI source and the deposition rate of the $PbI_2$ source are controlled by a proportional-integral-derivative (PID) controller to be varied as desired. Once these variables are constant, in the second stage of the process, we open the shutter near the substrate to start the deposition of the perovskite film. Finally, in the third stage, we close all shutters to control the thickness of the perovskite film, and allow the sources to cool down below 100 °C before refilling the chamber with nitrogen and opening the chamber.

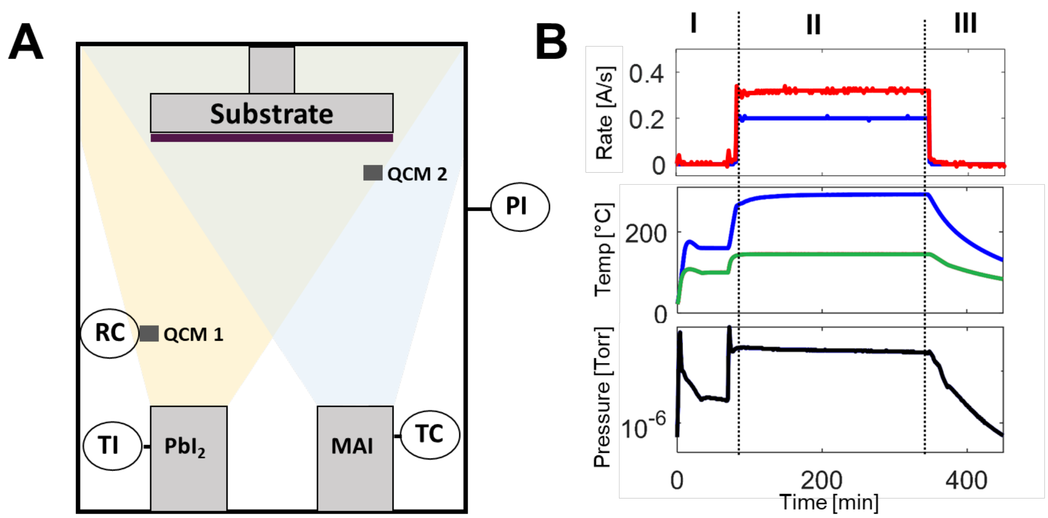


**Figure 1.** Schematic of the process. A. Vacuum chamber and components. B. Variables over time indicating the precondition step (I), deposition step (II), and cool down (III). The signals in the figure are color coded. Red: QCM substrate. Blue: QCM and Temperature $PbI_2$. Green: Temperature MAI. Black: Chamber pressure.

Devices were fabricated with a flat n-i-p architecture using $TiO_2$ as the electron transport material and spiro-OMeTAD as the hole transport material. FTO glasses were cleaned by sonicating 15 min in a 2% Hellmanex solution, distilled water, acetone, and isopropyl alcohol. The layer of compact-$TiO_2$ was deposited by spray pyrolysis using a solution that contains 10.8 mL of Ethanol (Sigma), 480 µL of acetylacetone (Sigma), and 720 µL of titanium diisopropoxide bis(acetylacetonate) (75% in isopropyl alcohol, Sigma). The deposition was made in 7 cycles of 10 seconds of spraying separated by 30 seconds from each other. The substrates were held at 450 °C during deposition and left at 450 °C for 30 min after the deposition was completed. The perovskite film was deposited via thermal evaporation, as described above, varying the deposition rate of the MAI powders. The spiro-OMeTAD layer was made by spin coating as described elsewhere [32]. Finally, we used a 52 nm layer of gold as the back contact.

Film morphology was characterized using a SEM Hitachi SU8230, and average grain size was obtained by measuring 60 different grains from micrographs taken with a magnification of 50k with ImageJ. The grain size was measured as the distance of a line that connects two sides and crosses the center of the grain. The UV-Vis absorption spectra were acquired with a Cary 5000 UV-Vis/NIR spectroscope. The steady state photoluminescence was taken in a Horiba FL3-21 Fluorometer. X-ray diffraction measurements were done in ambient in a PANalytical Empyrean using Gonio scans from 5° to 60°. GIWAXS measurements were taken at beamline 11-BM of the National Synchrotron Light Source II (NSLS-II) in Brookhaven National Laboratory on perovskite films deposited on FTO cut to a size of 0.5 cm x 0.5 cm. The samples were measured at four different incident angles from 0.05° to 0.5° with 10 seconds of exposure time. The x-ray beam had an energy of 13.5 keV, 0.2 mm (height) x 0.05 mm (width) size, 1 mrad divergence and an energy resolution of 0.7%. X-ray fluorescence (XRF) microscopy measurements were conducted using Advanced Photon Source (APS) at beamline 2-ID-D in Argonne National Laboratory. The 13.8 keV X-ray was focused using Fresnel zone plate with 300 nm FWHM. Data were analyzed using the SciAnalysis python library provided by the beamline. Solar cell photovoltaic parameters were extracted from current-voltage (JV) characteristics collected with a Fluxim solar simulator under AM1.5G illumination, using a scan rate of 50 mV/s. JV curves were acquired in forward and reverse, and a stabilized PCE was taken from a maximum power point track (mppt) of 5 min.

## Results and Discussion

To understand the growth mechanisms of $MAPbI_3$ by evaporation, we deposited films with a constant rate of $PbI_2$ at 0.2 Å/s and varying the temperature of the MAI source from 80 °C to 170 °C. Figure 2A shows a series of the deposited films, where it is seen that for source temperatures below 140 °C, films resemble the color of the $PbI_2$ precursor with a slight increase in opacity as temperature increases. As the temperature reaches 140 °C, a sudden change in color is observed towards the deep brown tint typical of $MAPbI_3$. As the temperature increases beyond 140 °C, more MAI becomes available in the chamber to react with $PbI_2$, which is associated with a further darkening of the films. Notably, the deposited film color drastically lightens at a MAI source temperature of 170 °C, which could be related to a large excess of MAI impeding the crystallization of the film. The ultraviolet-visible absorption (UV-vis, Figure 2B) of these films highlights the existence of the $MAPbI_3$ perovskite phase when the MAI source temperature is held between 140 and 165 °C, as shown by the onset in the spectrum at 750 nm. At 120 °C the absorption is dominated by $PbI_2$, with an onset around 510 nm as well as at lower MAI source temperatures as Figure S2 shows. At 170 °C the absorption of the film drops significantly, suggesting no conversion to a perovskite phase occurs in the presence of a large excess of MAI.

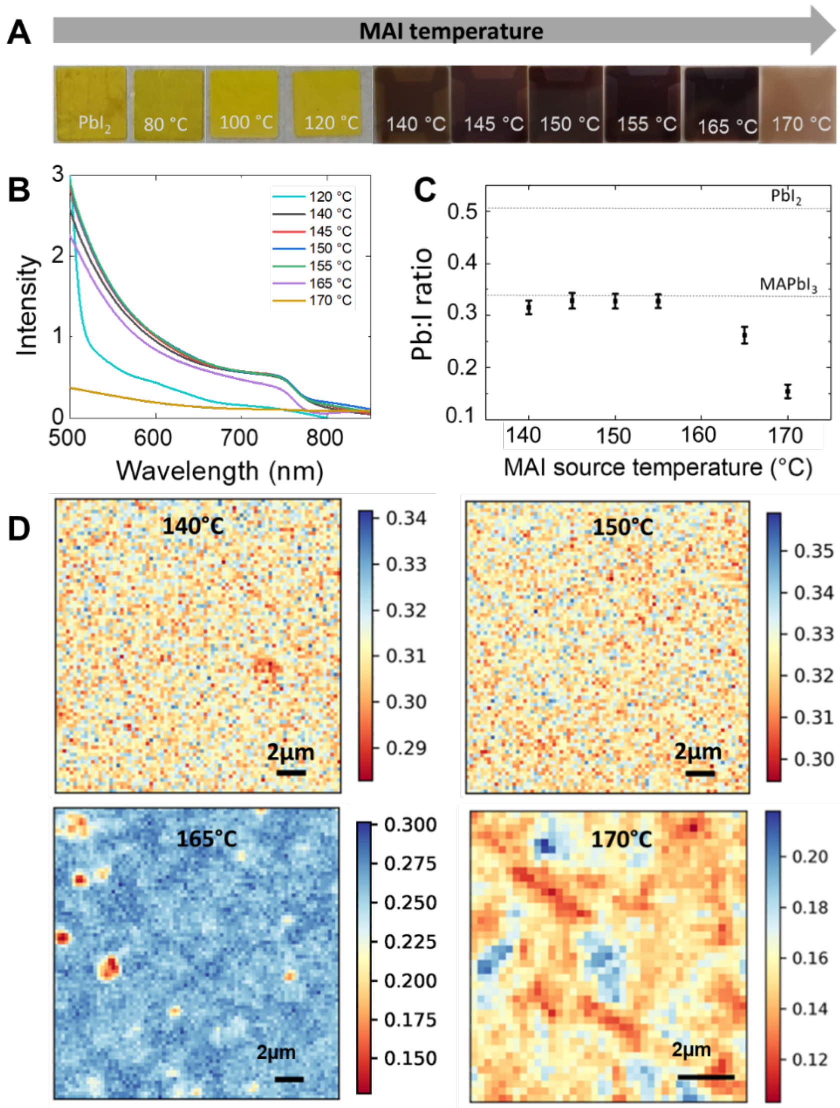


**Figure 2.** Optical properties and chemical composition of co-evaporated films at a constant $PbI_2$ rate of 0.2 Å/s and varying MAI source temperature. A) Photographs of the layers. B) UV-VIS absorption spectra of the films deposited with MAI source temperatures between 120 °C and 170 °C. C) Pb:I molecular ratio calculated from XRF maps of 100 µm x 100 µm. D) Pb:I ratio XRF maps with 250 nm step size/ pixel.

The changes observed in the optical properties of the layers are closely related to the overall stoichiometry of the films. Figure 2C shows the Pb:I molecular ratio calculated from the XRF maps taken in an area of 100 µm x 100 µm (maps in Figure S3). In addition, Figure 2D shows Pb:I ratio X-ray fluorescence mapping of samples processed at selected MAI source temperatures. We observed that films with MAI source temperatures from 140 °C to 155 °C are homogeneous in the scanned areas, and the Pb:I ratio is close to the theoretical value of 0.33 for $MAPbI_3$. On the other hand, at MAI temperature of 165 °C, small domains of a few microns with low Pb:I ratio are formed, which also decreases the average Pb:I ratio of the film. These domains are believed to be segregation of MAI or the formation of low dimensional perovskite phases, as discussed below. At a MAI temperature of 170 °C, the film has larger domains with low content of Pb, and even the maximum Pb:I ratio in the map (1:5) is far from the theoretical ratio of $MAPbI_3$ (1:3). This information suggests that at lower source temperatures, MAI can only significantly sorb to the substrate when it interacts with $PbI_2$ to form a perovskite phase. For this reason, there is a region between 140 °C and 155 °C that has a constant Pb:I ratio close to stoichiometric, as there is enough MAI to fully convert the flux of $PbI_2$, but no excess of MAI remains in the film. However, at higher temperatures, where the MAI evaporation rate increases more, the amount of MAI molecules interacting with the substrate is high. For instance, sorption to the fully converted perovskite can be observed even though the sticking factor of MAI to itself or perovskites is low compared to the sticking factor to $PbI_2$. This trend at higher temperature is confirmed by the XRF of the films (Figure 2C), which shows there is an excess of MAI in the film at 170 °C MAI source temperature. In general, this behavior agrees with reports that show that the low sticking factor of MAI makes it difficult to form MAI-only films on QCM's, and that the sticking factor strongly depends on the substrate material [33,34]. Figure S5 shows XRF maps obtained with films evaporated at a higher deposition rate of 1.16 Å/s. We observed that with higher flux of $PbI_2$, the formation of Pb-poor domains is only observed at the highest temperature (170 °C) and contrary to the deposition rate of 0.2 Å/s, the Pb:I ratio constantly decreases from a Pb-rich to a Pb-poor without a region of stoichiometric films. This shows that to obtain a region of stoichiometric films with different MAI source temperatures, the $PbI_2$ deposition rate must be low. It is necessary to have enough MAI evaporation rate to react with all the $PbI_2$, but not enough MAI evaporation rate to significantly sorb to the substrate after all the $PbI_2$ has been converted to the perovskite structure.

Figure 3 shows the proposed mechanism for the formation of the evaporated films with a $PbI_2$ deposition rate of 0.2 Å/s that is divided into three regions. In the first region where the MAI source temperature below 140 °C, MAI only significantly adsorbs to the substrate when it reacts with a molecule of $PbI_2$ on the substrate. Due to the low MAI evaporation rate, the flux of $PbI_2$ is not fully converted to perovskite. In this region, the Pb:I ratio will continuously decrease as the evaporation rate of MAI increases. The formation of $PbI_2$ rich film at temperature below 140 °C is corroborated by the UV-VIS of these films, where $PbI_2$ dominates the absorption of the films (Figure S2). In the second region, for temperatures between 140 °C and 155 °C, the evaporation rate of MAI is enough to convert all the flux of $PbI_2$ into the perovskite, but condensation of MAI on the substrate is not significant as the evaporation rate is still low. In this region, the Pb:I ratio is independent of the MAI evaporation rate and close to 1:3. Lastly, in the third region, for temperatures above 155 °C, we expect the accumulation of MAI on the substrate as the evaporation rate is high enough for molecules of MAI to adsorb to other molecules of MAI and/or to $MAPbI_3$. However, we expect that as the $PbI_2$ deposition rate increases, the range of temperature at which it is possible to obtain stoichiometric films is shortened. Figure S5 shows the comparison of the hypothesized behavior for different $PbI_2$ deposition rates. At high $PbI_2$ deposition rates, this region disappears, and as result, the Pb:I always decreases with the increase of MAI evaporation rate.

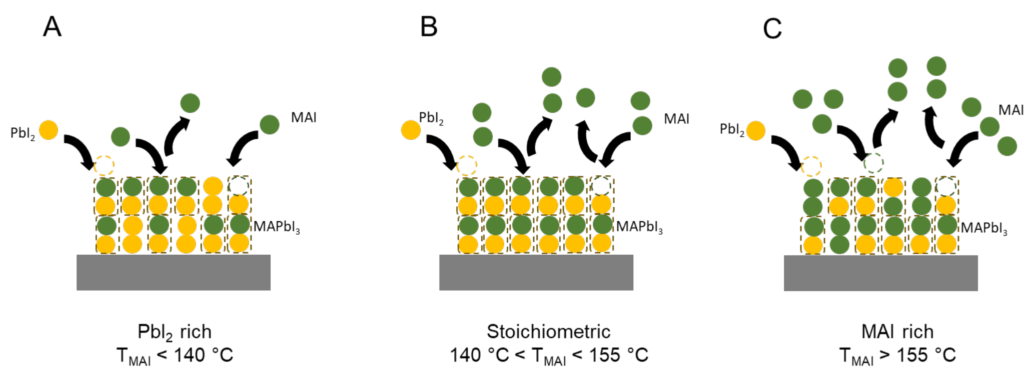


**Figure 3.** Schematic of the proposed stoichiometries of evaporated $MAPbI_3$ films with varying MAI source temperature. A) Low-temperature MAI-limiting region: An increase in the MAI evaporation rate

also increases the amount of MAI incorporated in the film. B) $PbI_2$-limiting region: The amount of MAI incorporated in the film remains constant as the flux of $PbI_2$ is fully converted, and molecules of MAI do not stick well to the substrate. C) High-temperature MAI-limiting region: The MAI evaporation rate is high and the amount of MAI molecules that remain in the substrate is significant.

In addition to the stoichiometry of the film, the amount of evaporated MAI, controlled by the temperature of the MAI source, also influences the layer's morphology. The SEM images of $MAPbI_3$ films deposited with different MAI source temperatures are presented in Figure 4. All films are pinhole-free and are distinguished by small grains with narrow distribution. The apparent grain sizes (as identified from SEM) were dependent on the MAI source temperature and increased from an average of 39 nm at 140 °C to 131 nm at 165 °C. Films deposited at 170 °C, on the other hand, have a different morphology. These films are rougher, and the shape of the apparent grains is less defined than at lower temperatures.

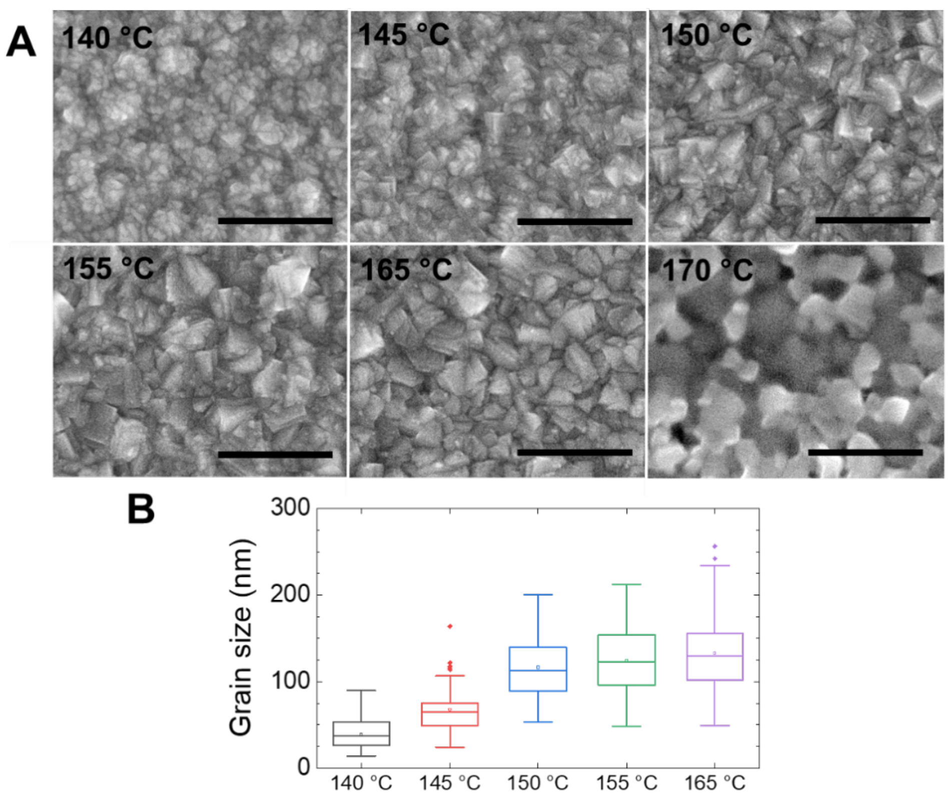


**Figure 4.** SEM images of films deposited with a constant deposition rate of $PbI_2$ of 0.2 Å/s and different temperatures (A) and average grain size (B). The scale bar is 500 nm in all the images.

The observed grain size dependence on temperature agrees with previous studies on co-evaporated $MAPbI_3$[35–37]. Arivazhagan et al[28] showed that grain size could be optimized by balancing the stoichiometry of the film and found that it was possible to achieve grains of more than 1 µm under optimized conditions. Likewise, Hsiao et al.[38] controlled the grain size of $MAPbI_3$ layers in a two-step evaporation method by changing the vapor pressure of MAI at which the layer of $PbI_2$ was exposed. In these studies, smaller grains are related to an excess of either $PbI_2$ or MAI in the film. On the other hand, Lohmann et al[17] showed that grain size also depends on the substrate temperature, being able to achieve grains of several microns when the substrate is held at -2 °C during deposition. They suggest that the growth mechanism begins with the deposition of $PbI_2$ on the substrate, which thereafter reacts with MAI, similar to the work by Kim et al[34]. Rapid conversion of $PbI_2$ to perovskite is important in the formation of larger grains, and this can be achieved at lower substrate temperatures due to the increase in MAI adsorption rate. Nevertheless, they observed higher device efficiency on films that were deposited at room temperature, despite smaller grains, suggesting a lack of understanding of other dominating effects [39]. Here we show that although the overall composition of the films does not change for MAI temperature between 140 °C and 155 °C, the grain size increases. Therefore, the evaporation rate of MAI plays a role in the growth mechanism of the crystals different than only determining the stoichiometry of the films.

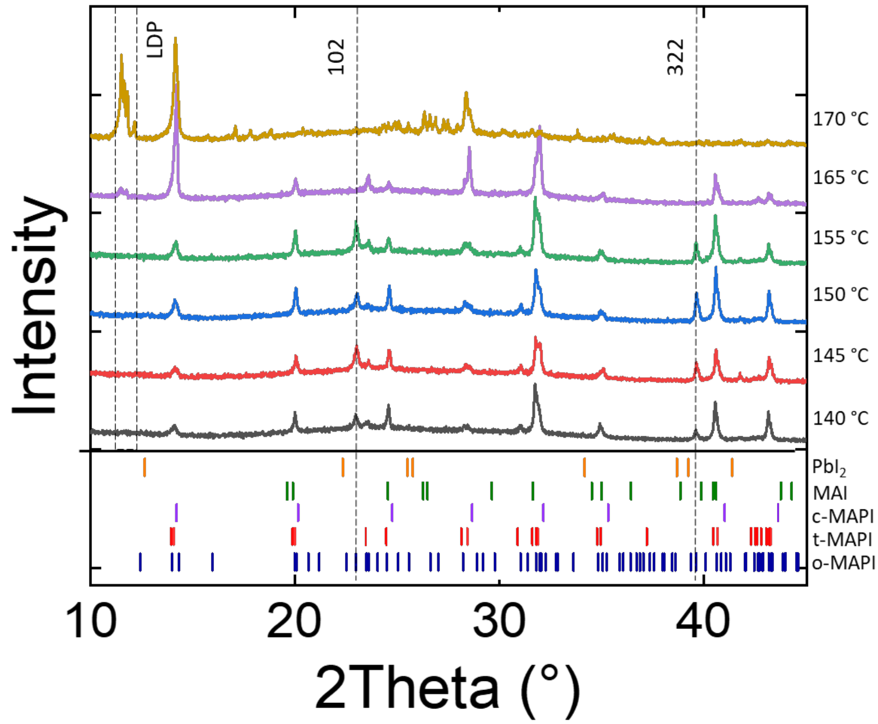


**Figure 5.** Top: XRD pattern of evaporated samples using constant deposition rate of $PbI_2$ of 0.2 Å/s. Bottom: Simulated diffraction peaks for precursors and different phases of $MAPbI_3$ (cubic *Pm3m*, tetragonal *I4/mcm*, and orthorhombic *Pnma*). The dotted lines indicate diffraction planes of orthorhombic phase, and low dimensional perovskite (LDP).

To understand the effect of MAI temperature on perovskite crystallinity, we measured the XRD pattern of the films. Figure 5 shows the XRD patterns of the films deposited with temperatures between 140 °C and 170 °C and a constant deposition rate of $PbI_2$ of 0.2 Å/s. Lower temperatures are shown in Figure S7. Films processed with MAI source temperatures below 120 °C only show peaks related to $PbI_2$, but at higher temperatures, peaks that correspond to $MAPbI_3$ emerged in the pattern. This corroborates our analysis on the stoichiometry of the film (proposed mechanism in Figure 3) as the XRD data is in line with the UV-VIS and XRF data discussed previously. Nonetheless, we observed variations in the relative intensity of $MAPbI_3$ XRD peaks as the evaporation rate of MAI increased by using higher temperature of MAI. For temperatures between 140 °C and 155 °C, the most intense peak is at $2\theta = 31.7°$, but at 165 °C, the most intense peak is found at 2θ = 14.2°. These changes in the relative intensity may be related to changes in the preferred crystallographic orientation of the film and to the formation of different crystalline phases. Interestingly, we observe that films with temperatures below 165 °C have two distinguishable peaks that match with an orthorhombic Pnma phase at 2θ = 22.98°, and 39.6°, for the (102), and (322) planes, respectively. These peaks disappear at 165 °C, suggesting that our films are composed of a mixture of crystalline phases, and that the ratio between the two different phases depends on the source temperature of MAI.

Studies on $MAPbI_3$ evaporation typically do not focus on the crystallographic variations induced by changes in the deposition parameters. We found that in most studies, the diffraction pattern only shows two predominant peaks at 2θ = 14.1° and 28.4°, that are indexed to either the (110) and (220) planes of the tetragonal phase[35,40,41] or the (100) and (200) of the cubic phase[36]. Palazon et al.[42] studied these two XRD peaks on films deposited at room temperature with different $PbI_2$ deposition rates. They found that a lower deposition rate of $PbI_2$ forms a tetragonal phase with peaks for the (002) and (110) planes at 2θ = 14.0° and 14.1°. On the other hand, higher deposition rates allow the formation of a cubic phase, showing only one peak at 2θ = 14.2° that corresponds to the (100) plane. However, none of these studies observe the formation of a secondary phase in the perovskite film. This may be due to the different rates of $PbI_2$ evaporation used in the literature which leads to formation of perovskites with pure tetragonal phases. In our study, we found that changing the evaporation rate from 0.2 Å /s to 1.0 Å /s leads to suppression of the secondary phase as shown in Figure S8.

To further understand the XRD data with respect to different phases, we performed a Le Bail refinement using FullProf Suite with an orthorhombic (P n m a) and a tetragonal (I 4/m c m) structure. Figure 6 shows a comparison of the refinement around these peaks for films evaporated with MAI source temperature of 145 °C and 165 °C. We found that at lower temperatures, the simulation with the fitted tetragonal phase cannot explain the presence of the peaks at $2\theta = 22.98°$ and 39.6°, whereas the simulation of the orthorhombic phase fits both peaks (Figure 6B and 6C, 145 °C). At lower temperatures, the lattice parameters *b* and *c* of the orthorhombic phase are different than the ones of the tetragonal phase, indicating two different crystal phases. At 165 °C, the fitted tetragonal and orthorhombic phase have similar *a, b*, and *c* lattice parameters, evidence of only one crystal phase. The full range of the refinement and the analysis of the additional temperatures is shown in figure S13. In the case of the films deposited with a MAI source temperature of 170 °C, we found that none of the perovskite structures can reproduce the XRD pattern, suggesting the formation of an amorphous or non-perovskite material.

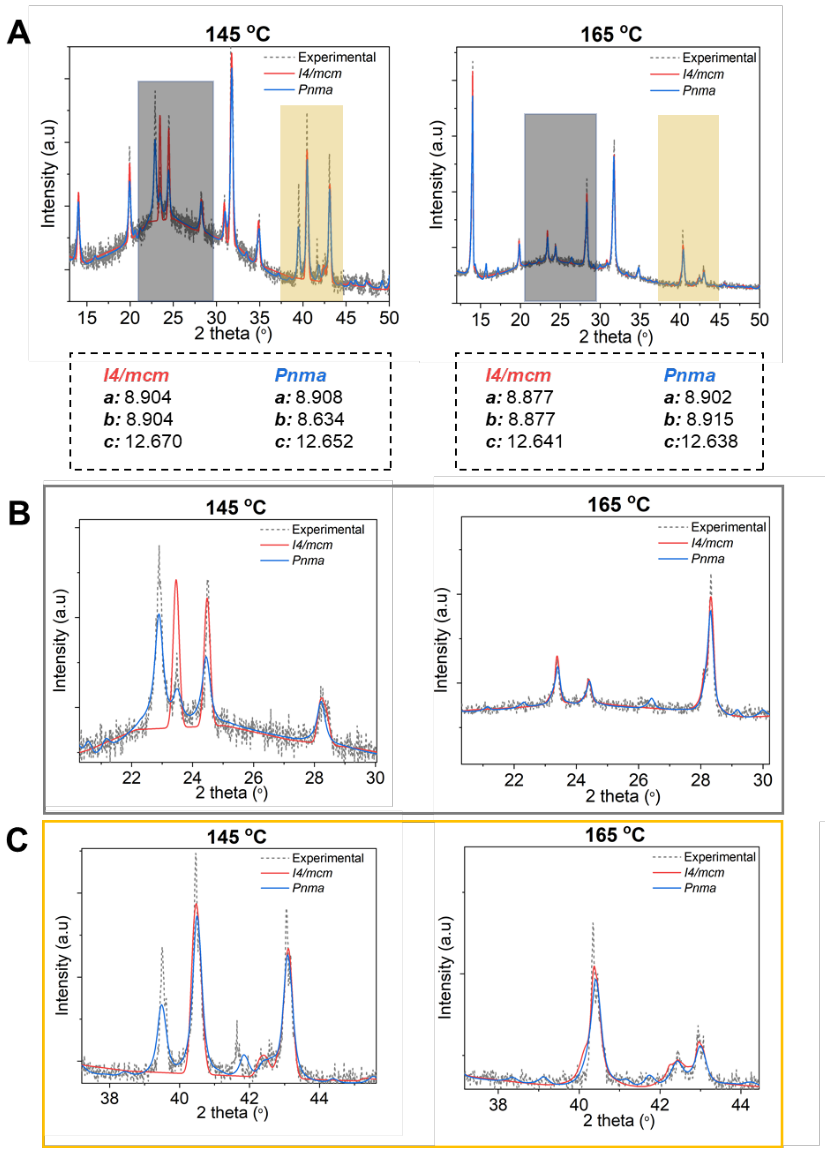


**Figure 6.** Le Bail refinement of selected XRD diffraction patterns of films deposited with MAI source temperature of 145 °C and 165 °C, and constant $PbI_2$ rate of 0.2 Å /s. A) Complete pattern. B) Amplified region from 2θ=20° to 2θ=30°. C. Amplified region from 2θ= 37° to 2θ=44°.

To corroborate the crystallographic changes that we see in XRD and to provide additional insight, we performed GIWAXS on films deposited with MAI temperature from 140 °C to 170 °C. Complementary to XRD, GIWAXS allows to see all diffraction peaks generated by our perovskite thin films, regardless of preferred crystallographic orientation. Figure 7 shows the circular average obtained from the 2D patterns. We compared the diffraction peaks to the position of the peaks in the precursors and the three crystallographic phases of $MAPbI_3$, as we can see in Figure S9 to S14. $PbI_2$ is present in the films at temperatures below 165 °C, although the relative intensity of $PbI_2$ peaks decreased significantly as the MAI source temperature increased. In terms of perovskite structures in the films, we observed that a MAI temperature from 140 °C to 165 °C leads to the formation of a perovskite structure. The three crystallographic phases (cubic, tetragonal, and orthorhombic) of $MAPbI_3$ have peaks with a similar position, which make it difficult to determine if multiple phases are present in the films. However, similar to the XRD, the peaks for the planes (102) and (322), at q values equal to 1.68 $Å^{-1}$ and 2.76 $Å^{-1}$ respectively, are distinguishable at lower temperature, and its intensity decreases as the temperature of the MAI source increases. Moreover, the peaks for the planes (132) and (401)/(004) of the orthorhombic phase at q values equal to 2.20 $Å^{-1}$ and 2.92 $Å^{-1}$, respectively, which are not visible in the XRD, can also be seen in the pattern, and its intensity decreases as the temperature of the MAI source increases. This corroborates our hypothesis that a secondary phase is present in the films with a Pnma space group as shown in the LeBail refinement. A higher evaporation rate of MAI prevents the formation of these secondary phases. In samples with MAI source temperature spanning from 155 °C to 165 °C, we observe dominant diffraction from either the tetragonal or the cubic phase. The accurate distinction between these two phases is difficult due to the lower angular resolution typical of the grazing incidence measurement configuration. Nonetheless, XRD showed that tetragonal phase is dominant at 165 °C.

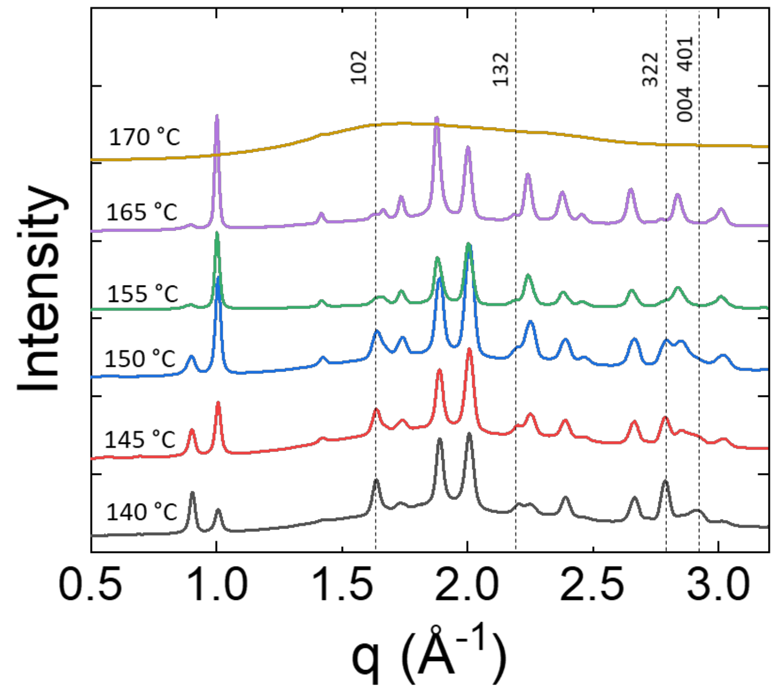


**Figure 7.** Circular integration of GIWAXS pattern of perovskite films for different MAI temperatures. The location of planes of the orthorhombic phase that are distinguishable from the cubic and tetragonal phases is marked dotted lines in the graph.

It is worth noting that studies on the phase transitions of $MAPbI_3$ show that the orthorhombic phase is stable at temperature below -111°C, the tetragonal phase between -111°C and 56.8 °C, and the cubic phase at above 56.8 °C[43–45], which raises questions on how either the orthorhombic or cubic phase can grow in a substrate that is at room temperature. As discussed before, some studies have suggested that the cubic phase may form at room temperature when the perovskite layer is deposited through vapor deposition, and that the layer is stable even under atmospheric conditions. This was possible by increasing the $PbI_2$ deposition rate to 0.5 Å/s. For lower $PbI_2$ deposition rates, they obtained a tetragonal phase[42], which has lower symmetry. However, the temperature range for the orthorhombic phase is far from the processing temperature in thermal evaporation, and thermal energy from the vapor phase would provide energy to the film, which would undermine the presence of the orthorhombic phase.

Another possibility is that these peaks come from low dimensional non-perovskites (LDP), such as so-called 2D, 1D, or 0D perovskites. Evidence of these LDP and stacking faults have been shown before by kelvin probe force microscopy (KPFM)[29], showing that a co-evaporated $MAPbI_3$ film may contain traces of these phases. However, their study also shows that these phases are obtained especially at high MAI partial pressures in the chamber, which means a higher evaporation rate of MAI. Excess of MAI in the perovskite film causes issues with the stack of single layers of $PbI_4^-$ octahedra, exfoliating them and forming a 2D or lower dimension arrangement instead of the 3D perovskite [46]. Nonetheless, our experiments show that the films that contains orthorhombic crystals were deposited using a lower temperature of MAI, lower evaporation rate, and XRF shows that the overall stoichiometry of these films is close to stoichiometric $MAPbI_3$. Moreover, LDP can be distinguished by the formation of peaks in the XRD at low angles (around 11.5°), which are also absent in samples at temperature below 155 °C. However, it is worth noting that the XRD of films at 165 °C show a small content of LDP that increases at MAI source temperature of 170 °C, which corroborates the relationship between LDP and an excess of MAI during deposition.

The Le Bail refinement suggests that the observed secondary phase belong to the Pnma space group. However, the XRD patterns were taken from thin films, which causes the absence of predominant peaks of an orthorhombic $MAPbI_3$ perovskite, such as the peak for the (202) plane at $2\theta$ equals to 28.9° or q equals to 2.03 $Å^{-1}$. Likewise, the lower angular resolution of GIWAXS makes it difficult to distinguish this peak, and other predominant peaks of the orthorhombic phase, since they overlap with those for the cubic and tetragonal phases. Nonetheless, density functional theory (DFT) studies on perovskites show that it is possible to obtain orthorhombic $MAPbI_3$ stable under certain conditions. For example, Yang et al.[47] calculated the formation energy of orthorhombic $MAPbI_3$ to be negative at room temperature, meaning that this phase can be thermodynamically stable. Therefore, this provides additional support for the explanation of our XRD and GIWAXS data showing an orthorhombic $MAPbI_3$ perovskite phase. However, it is not possible to definitively state that we have an orthorhombic $MAPbI_3$ perovskite structure, since the XRD and GIWAXS predominant peaks cannot unequivocally be detected or indexed. Instead, we can be certain that we have a secondary phase that fits an orthorhombic phase with a Pnma space group. Figure 8 shows a schematic of the effect of the MAI source temperature on the crystallinity of the deposited film.

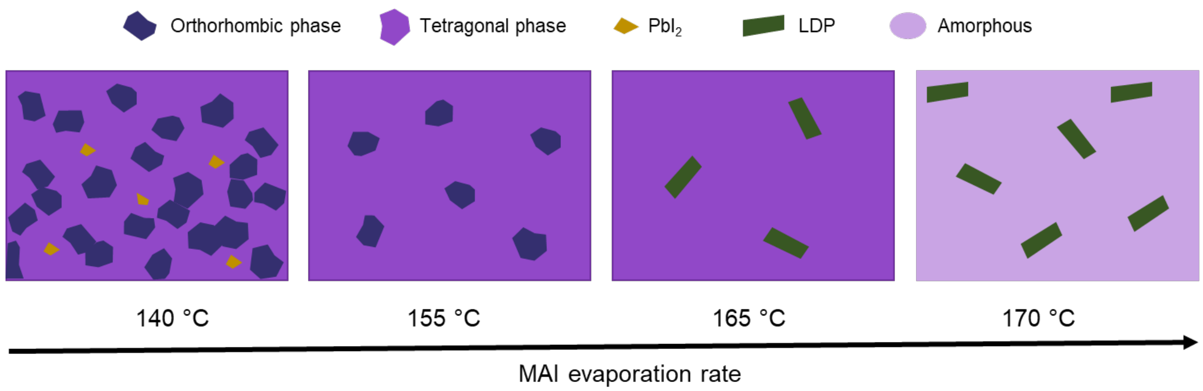


**Figure 8.** Macroscale schematic of the crystallographic dependence of the MAI evaporation rate on the evaporated perovskite layer.

To understand the impact of crystallographic and compositional changes on the performances of complete devices, we fabricated solar cells in flat n-i-p architecture using c-$TiO_2$ deposited by spray pyrolysis as electron transport layer and spiro-OMeTAD as hole transport material. Figure 9 shows the performance parameters of devices made using MAI source temperatures from 140 °C to 170 °C to deposit the perovskite layer. We obtain a maximum PCE of 12.13% using 165 °C as MAI source temperature, as opposed to a maximum PCE of 8.09% on reference devices with $MAPbI_3$ deposited via solution in the same architecture. We note that the limited PCE is to be attributed to not having a mesoporous $TiO_2$ layer in the devices (Figure S18) and not to a low quality of the deposited perovskite. Similar PCEs obtained with the two different deposition methods on the same architecture thus hint for similar optoelectronic properties of the processed $MAPbI_3$ films. A further improvement in efficiency might be pursued by optimizing a different planar electron selective layer. $SnO_2$ and C60 has exhibit promising results in flat architectures devices compared to c-$TiO_2$, which has an energetic mismatch with some perovskite compositions[51]. However, this is beyond the scope of the present work.

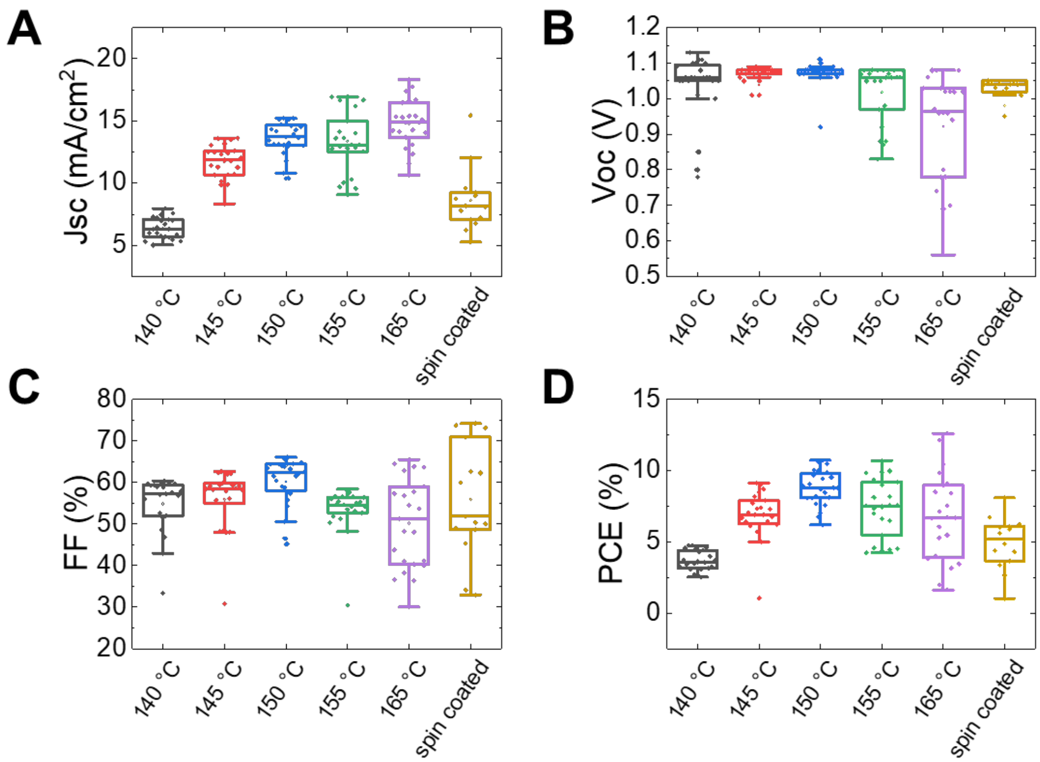


**Figure 9.** Device performance of devices varying temperature of MAI source and including a solution-processed device of reference. A) Short-circuit current. B) Open circuit voltage. C) Fill factor. D) Power conversion efficiency

The performances of the devices reflect the changes in the crystallinity of the perovskite layer. Figure 9A shows that lower MAI temperature exhibits lower short circuit current density ($J_{SC}$). The absorption spectra in Figure 2 show that all films with temperature from 140 °C to 155 °C absorb the same light, and the film with 165 °C, which indeed produce the highest current, has lower absorption. For this reason, it suggests that a lower current in the devices is related to the presence of a secondary phase in the film when low MAI evaporation rates are used, which can limit the transport of charges in the perovskite films and favor recombination before extraction. A comparison of samples at 145 °C and 150 °C reinforces this premise. XRF shows nearly identical stoichiometry, but both $J_{SC}$ and fill factor (*FF*) increase as the secondary phase peaks in XRD and GIWAXS decrease. Grain boundaries can also contribute to charge transport losses. Figure 3 shows that the average grain size increases with the temperature of MAI. However, we do not expect changes in the performance of the devices due to changes in the grain size as grain boundaries have a minimal impact in the performance, as shown in the literature [52].

Figure 9B shows that the open-circuit voltage ($V_{OC}$) is affected. Higher evaporation rates of MAI produce devices with lower $V_{OC}$. From the time resolved photoluminescence (TrPL) and steady-state PL data (Figure S19), we expected to see the highest $\mathrm{V_{OC}}$ in the sample with a MAI temperature of 165 °C. However, XRD and XRF showed that, at this temperature, the film contains small quantities of LDP. LDP can form traps that enhance recombination in the film and has been associated with induced strain in the lattice of the material upon illumination (photostriction). Photostriction has been shown to enhance degradation due to penetration of water at a higher speed, and thus lower the performance of the solar cell[29].

**Conclusions**

In this work, we found that evaporation rate of MAI, controlled by varying the temperature of the MAI source, influences not only the stoichiometry of thermally evaporated perovskite films, but it also determines the crystalline properties of the film. We showed that a lower temperature of the MAI source (less than 155 °C) combined with a $PbI_2$ deposition rate of 0.2 Å/s induces the formation of a secondary phase, possibly with a Pnma space group, in addition to the $MAPbI_3$ tetragonal structure. Increasing the MAI source temperature to 165 °C increases the purity of the deposited $MAPbI_3$ film, which fits into the tetragonal structure as shown by Le Bail refinement. Nonetheless, increasing the MAI source temperature also plays a role in the formation of low dimensional phases, which can be seen in both XRF maps and XRD patterns for 165 °C and 170 °C. These changes in the purity of the films are reflected in the performance of the fabricated devices. Overall, we associate the presence of the secondary phase to charge transport losses that influence the $J_{SC}$ of the devices, and the presence of LDP to recombination that lowers the $V_{OC}$. This work provides a path forward to the deposition of MAPbI3 by thermal evaporation, where an interplay between $PbI_2$ and MAI deposition rates is crucial to the properties of the materials.

**Acknowledgments**

A.F.C.M. thanks Esteban Rojas-Gatjens and Carlos Silva for their help with tr-PL experiments. This work was performed in part at the Georgia Tech Institute for Electronics and Nanotechnology, a member of the National Nanotechnology Coordinated Infrastructure (NNCI), which is supported by the National Science Foundation (Grant ECCS-1542174). A.F.C.M. received funding from the Colombian Ministry of Sciences and Technology and the U.S. Department of State under a Fulbright Scholarship. J.H. and J.V. received funding from the Department of Education Graduate Assistance in Areas of National Need (GAANN) program at Georgia Institute of Technology (Award # P200A180075).

**Supporting information**

Additional information related to this article, including XRD diffraction patterns, XRF maps, UV-VIS absorption spectra, photoluminescence data, and X-ray photoelectron spectroscopy, can be found in the supporting information.

**References**

(1) Kojima, A.; Teshima, K.; Shirai, Y.; Miyasaka, T. Organometal Halide Perovskites as Visible-Light Sensitizers for Photovoltaic Cells. *J. Am. Chem. Soc.* **2009**, *131* (17), 6050–6051. https://doi.org/10.1021/ja809598r.

(2) NREL. Best Research-Cell Efficiencies. U.S. Department of Energy.

(3) Kim, M.; Kim, G. H.; Lee, T. K.; Choi, I. W.; Choi, H. W.; Jo, Y.; Yoon, Y. J.; Kim, J. W.; Lee, J.; Huh, D.; Lee, H.; Kwak, S. K.; Kim, J. Y.; Kim, D. S. Methylammonium Chloride Induces Intermediate Phase Stabilization for Efficient Perovskite Solar Cells. *Joule* **2019**, *3* (9), 2179–2192. https://doi.org/10.1016/j.joule.2019.06.014.

(4) Jiang, Q.; Zhao, Y.; Zhang, X.; Yang, X.; Chen, Y.; Chu, Z.; Ye, Q.; Li, X.; Yin, Z.; You, J. Surface Passivation of Perovskite Film for Efficient Solar Cells. *Nat. Photonics* **2019**, *13* (7), 460–466. https://doi.org/10.1038/s41566-019-0398-2.

(5) Jeon, N. J.; Na, H.; Jung, E. H.; Yang, T. Y.; Lee, Y. G.; Kim, G.; Shin, H. W.; Il Seok, S.; Lee, J.; Seo, J. A Fluorene-Terminated Hole-Transporting Material for Highly Efficient and Stable Perovskite Solar Cells. *Nat. Energy* **2018**, *3* (8), 682–689. https://doi.org/10.1038/s41560-018-0200-6.

(6) Jung, E. H.; Jeon, N. J.; Park, E. Y.; Moon, C. S.; Shin, T. J.; Yang, T. Y.; Noh, J. H.; Seo, J. Efficient, Stable and Scalable Perovskite Solar Cells Using Poly(3-Hexylthiophene). *Nature* **2019**, *567* (7749), 511–515. https://doi.org/10.1038/s41586-019-1036-3.

(7) Basumatary, P.; Agarwal, P. Two-Step Fabrication of MAPbI 3 Perovskite Thin Films with Improved Stability. *Bull. Mater. Sci.* **2019**, *42* (6), 268. https://doi.org/10.1007/s12034-019-1959-1.

(8) Wang, L.; Wang, X.; Deng, L. L.; Leng, S.; Guo, X.; Tan, C. H.; Choy, W. C. H.; Chen, C. C. The Mechanism of Universal Green Antisolvents for Intermediate Phase Controlled High-Efficiency Formamidinium-Based Perovskite Solar Cells. *Mater. Horizons* **2020**, *7* (3), 934–942. https://doi.org/10.1039/c9mh01679a.

(9) Yang, D.; Yang, R.; Priya, S.; Liu, S. (Frank). Recent Advances in Flexible Perovskite Solar Cells: Fabrication and Applications. *Angew. Chemie* **2019**, *58* (14), 4466–4483. https://doi.org/10.1002/ange.201809781.

(10) Nayak, P. K.; Mahesh, S.; Snaith, H. J.; Cahen, D. Photovoltaic Solar Cell Technologies: Analysing the State of the Art. *Nat. Rev. Mater.* **2019**, *4* (4), 269–285. https://doi.org/10.1038/s41578-019-0097-0.

(11) Gil-Escrig, L.; Dreessen, C.; Kaya, I. C.; Kim, B.-S.; Palazon, F.; Sessolo, M.; Bolink, H. J. Efficient Vacuum-Deposited Perovskite Solar Cells with Stable Cubic FA1–XMAxPbI3. *ACS Energy Lett.* **2020**, *5* (9), 3053–3061. https://doi.org/10.1021/ACSENERGYLETT.0C01473.

(12) Gil-Escrig, L.; Dreessen, C.; Palazon, F.; Hawash, Z.; Moons, E.; Albrecht, S.; Sessolo, M.; Bolink, H. J. Efficient Wide-Bandgap Mixed-Cation and Mixed-Halide Perovskite Solar Cells by Vacuum Deposition. **2021**, *07*, 37. https://doi.org/10.1021/acsenergylett.0c02445.

(13) Burwig, T.; Fränzel, W.; Pistor, P. Crystal Phases and Thermal Stability of Co-Evaporated CsPbX3 (X = I, Br) Thin Films. *J. Phys. Chem. Lett.* **2018**, *9* (16), 4808–4813. https://doi.org/10.1021/ACS.JPCLETT.8B02059.

(14) Li, J.; Wang, H.; Chin, X. Y.; Dewi, H. A.; Vergeer, K.; Goh, T. W.; Lim, J. W. M.; Lew, J. H.; Loh, K. P.; Soci, C.; Sum, T. C.; Bolink, H. J.; Mathews, N.; Mhaisalkar, S.; Bruno, A. Highly Efficient Thermally Co-Evaporated Perovskite Solar Cells and Mini-Modules. *Joule* **2020**, 1–19.

https://doi.org/10.1016/j.joule.2020.03.005.

(15) Babaei, A.; Zanoni, K. P. S.; Gil-Escrig, L.; Pérez-del-Rey, D.; Boix, P. P.; Sessolo, M.; Bolink, H. J. Efficient Vacuum Deposited P-I-N Perovskite Solar Cells by Front Contact Optimization. *Front. Chem.* **2020**, *7*, 936. https://doi.org/10.3389/fchem.2019.00936.

(16) Pérez-Del-Rey, D.; Boix, P. P.; Sessolo, M.; Hadipour, A.; Bolink, H. J. Interfacial Modification for High-Efficiency Vapor-Phase-Deposited Perovskite Solar Cells Based on a Metal Oxide Buffer Layer. *J. Phys. Chem. Lett.* **2018**, *9* (5), 1041–1046. https://doi.org/10.1021/acs.jpclett.7b03361.

(17) Lohmann, K. B.; Patel, J. B.; Rothmann, M. U.; Xia, C. Q.; Oliver, R. D. J.; Herz, L. M.; Snaith, H. J.; Johnston, M. B. Control over Crystal Size in Vapor Deposited Metal-Halide Perovskite Films. *ACS Energy Lett.* **2020**, 710–717. https://doi.org/10.1021/acsenergylett.0c00183.

(18) De Souza, R. A.; Barboni, D. Iodide-Ion Conduction in Methylammonium Lead Iodide Perovskite: Some Extraordinary Aspects. *Chem. Commun.* **2019**, *55* (8), 1108–1111. https://doi.org/10.1039/c8cc09236b.

(19) Sung, J.; Schnedermann, C.; Ni, L.; Sadhanala, A.; Chen, R. Y. S.; Cho, C.; Priest, L.; Lim, J. M.; Kim, H. K.; Monserrat, B.; Kukura, P.; Rao, A. Long-Range Ballistic Propagation of Carriers in Methylammonium Lead Iodide Perovskite Thin Films. *Nat. Phys.* **2020**, *16* (2), 171–176. https://doi.org/10.1038/s41567-019-0730-2.

(20) Lee, H.; Gaiaschi, S.; Chapon, P.; Tondelier, D.; Bourée, J. E.; Bonnassieux, Y.; Derycke, V.; Geffroy, B. Effect of Halide Ion Migration on the Electrical Properties of Methylammonium Lead Tri-Iodide Perovskite Solar Cells. *J. Phys. Chem. C* **2019**, *123* (29), 17728–17734. https://doi.org/10.1021/acs.jpcc.9b04662.

(21) Ava, T. T.; Al Mamun, A.; Marsillac, S.; Namkoong, G. A Review: Thermal Stability of Methylammonium Lead Halide Based Perovskite Solar Cells. *Appl. Sci.* **2019**, *9* (1). https://doi.org/10.3390/app9010188.

(22) Xu, H.; Wu, Y.; Cui, J.; Ni, C.; Xu, F.; Cai, J.; Hong, F.; Fang, Z.; Wang, W.; Zhu, J.; Wang, L.; Xu, R.; Xu, F. Formation and Evolution of the Unexpected PbI2 Phase at the Interface during the Growth of Evaporated Perovskite Films. *Phys. Chem. Chem. Phys.* **2016**, *18* (27), 18607–18613. https://doi.org/10.1039/c6cp02737g.

(23) Shi, B.; Yao, X.; Hou, F.; Guo, S.; Li, Y.; Wei, C.; Ding, Y.; Li, Y.; Zhao, Y.; Zhang, X. Unraveling the Passivation Process of PbI2 to Enhance the Efficiency of Planar Perovskite Solar Cells. *J. Phys. Chem. C* **2018**, *122* (37), 21269–21276. https://doi.org/10.1021/acs.jpcc.8b08075.

(24) Kim, J.; Ho-Baillie, A.; Huang, S. Review of Novel Passivation Techniques for Efficient and Stable Perovskite Solar Cells. *Sol. RRL* **2019**, *3* (4), 1800302. https://doi.org/10.1002/solr.201800302.

(25) Chen, S.; Wen, X.; Yun, J. S.; Huang, S.; Green, M.; Jeon, N. J.; Yang, W. S.; Noh, J. H.; Seo, J.; Seok, S. Il; Ho-Baillie, A. Spatial Distribution of Lead Iodide and Local Passivation on Organo-Lead Halide Perovskite. *ACS Appl. Mater. Interfaces* **2017**, *9* (7), 6072–6078. https://doi.org/10.1021/acsami.6b15504.

(26) Kim, Y. C.; Jeon, N. J.; Noh, J. H.; Yang, W. S.; Seo, J.; Yun, J. S.; Ho-Baillie, A.; Huang, S.; Green, M. A.; Seidel, J.; Ahn, T. K.; Seok, S. Il. Beneficial Effects of PbI2 Incorporated in Organo-Lead Halide Perovskite Solar Cells. *Adv. Energy Mater.* **2016**, *6* (4), 1–8. https://doi.org/10.1002/aenm.201502104.

(27) Huang, L.; Dong, H.; Huo, N.; Zheng, Z.; Deng, H.; Zhang, G.; Cheng, Y.; Li, J. Deep Insights

into Interface Engineering by Buffer Layer for Efficient Perovskite Solar Cells: A First-Principles Study. *Sci. China Mater.* **2020**, No. April, 1–9. https://doi.org/10.1007/s40843-020-1322-2.

(28) Arivazhagan, V.; Xie, J.; Yang, Z.; Hang, P.; Parvathi, M. M.; Xiao, K.; Cui, C.; Yang, D.; Yu, X. Vacuum Co-Deposited CH3NH3PbI3 Films by Controlling Vapor Pressure for Efficient Planar Perovskite Solar Cells. *Sol. Energy* **2019**, *181* (January), 339–344. https://doi.org/10.1016/j.solener.2019.02.012.

(29) Gallet, T.; Poeira, R. G.; Lanzoni, E. M.; Abzieher, T.; Paetzold, U. W.; Redinger, A. Co-Evaporation of CH3NH3PbI3: How Growth Conditions Impact Phase Purity, Photostriction, and Intrinsic Stability. *ACS Appl. Mater. Interfaces* **2021**, *13* (2), 2642–2653. https://doi.org/10.1021/acsami.0c19038.

(30) Heinze, K. L.; Dolynchuk, O.; Burwig, T.; Vaghani, J.; Scheer, R.; Pistor, P. Importance of Methylammonium Iodide Partial Pressure and Evaporation Onset for the Growth of Co-Evaporated Methylammonium Lead Iodide Absorbers. *Sci. Reports* | **123AD**, *11*, 15299. https://doi.org/10.1038/s41598-021-94689-1.

(31) Teuscher, J.; Ulianov, A.; Müntener, O.; Grätzel, M.; Tétreault, N. Control and Study of the Stoichiometry in Evaporated Perovskite Solar Cells. *ChemSusChem* **2015**, *8* (22), 3847–3852. https://doi.org/10.1002/cssc.201500972.

(32) Hidalgo, J.; Perini, C. A. R.; Castro-Mendez, A. F.; Jones, D.; Köbler, H.; Lai, B.; Li, R.; Sun, S.; Abate, A.; Correa-Baena, J. P. Moisture-Induced Crystallographic Reorientations and Effects on Charge Carrier Extraction in Metal Halide Perovskite Solar Cells. *ACS Energy Lett.* **2020**, *5* (11), 3526–3534. https://doi.org/10.1021/acsenergylett.0c01964.

(33) Bækbo, M. J.; Hansen, O.; Chorkendorff, I.; Vesborg, P. C. K. Deposition of Methylammonium

Iodide: Via Evaporation-Combined Kinetic and Mass Spectrometric Study. *RSC Adv.* **2018**, *8* (52), 29899–29908. https://doi.org/10.1039/c8ra04851g.

(34) Kim, B.-S.; Sessolo, M.; Bolink, H. J. Deposition Kinetics and Compositional Control of Vacuum-Processed CH 3 NH 3 PbI 3 Perovskite. **2020**. https://doi.org/10.1021/acs.jpclett.0c01995.

(35) Liu, M.; Johnston, M. B.; Snaith, H. J. Efficient Planar Heterojunction Perovskite Solar Cells by Vapour Deposition. *Nature* **2013**, *501* (7467), 395–398. https://doi.org/10.1038/nature12509.

(36) Malinkiewicz, O.; Roldán-Carmona, C.; Soriano, A.; Bandiello, E.; Camacho, L.; Nazeeruddin, M. K.; Bolink, H. J. Metal-Oxide-Free Methylammonium Lead Iodide Perovskite-Based Solar Cells: The Influence of Organic Charge Transport Layers. *Adv. Energy Mater.* **2014**, *4* (15). https://doi.org/10.1002/aenm.201400345.

(37) Liang, G.; Lan, H.; Fan, P.; Lan, C.; Zheng, Z.; Peng, H.; Luo, J. Highly Uniform Large-Area (100 Cm2) Perovskite CH3NH3PbI3 Thin-Films Prepared by Single-Source Thermal Evaporation. *Coatings* **2018**, *8* (8), 256. https://doi.org/10.3390/coatings8080256.

(38) Hsiao, S.-Y.; Lin, H.-L.; Lee, W.-H.; Tsai, W.-L.; Chiang, K.-M.; Liao, W.-Y.; Ren-Wu, C.-Z.; Chen, C.-Y.; Lin, H.-W. Efficient All-Vacuum Deposited Perovskite Solar Cells by Controlling Reagent Partial Pressure in High Vacuum. *Adv. Mater.* **2016**, *28* (32), 7013–7019. https://doi.org/10.1002/adma.201601505.

(39) Jacobsson, T. J.; Correa-Baena, J. P.; Halvani Anaraki, E.; Philippe, B.; Stranks, S. D.; Bouduban, M. E. F.; Tress, W.; Schenk, K.; Teuscher, J.; Moser, J. E.; Rensmo, H.; Hagfeldt, A. Unreacted PbI2 as a Double-Edged Sword for Enhancing the Performance of Perovskite Solar Cells. *J. Am. Chem. Soc.* **2016**, *138* (32), 10331–10343. https://doi.org/10.1021/jacs.6b06320.

(40) Kim, B. S.; Kim, T. M.; Choi, M. S.; Shim, H. S.; Kim, J. J. Fully Vacuum-Processed Perovskite Solar Cells with High Open Circuit Voltage Using MoO3/NPB as Hole Extraction Layers. *Org. Electron.* **2015**, *17*, 102–106. https://doi.org/10.1016/j.orgel.2014.12.002.

(41) Gao, C.; Liu, J.; Liao, C.; Ye, Q.; Zhang, Y.; He, X.; Guo, X.; Mei, J.; Lau, W. Formation of Organic-Inorganic Mixed Halide Perovskite Films by Thermal Evaporation of PbCl2 and CH3NH3I Compounds. *RSC Adv.* **2015**, *5* (33), 26175–26180. https://doi.org/10.1039/c4ra17316c.

(42) Palazon, F.; Pérez-del-Rey, D.; Dänekamp, B.; Dreessen, C.; Sessolo, M.; Boix, P. P.; Bolink, H. J. Room-Temperature Cubic Phase Crystallization and High Stability of Vacuum-Deposited Methylammonium Lead Triiodide Thin Films for High-Efficiency Solar Cells. *Adv. Mater.* **2019**, *31* (39), 1902692. https://doi.org/10.1002/adma.201902692.

(43) Pistor, P.; Burwig, T.; Brzuska, C.; Weber, B.; Fränzel, W. Thermal Stability and Miscibility of Co-Evaporated Methyl Ammonium Lead Halide (MAPbX3, X = I, Br, Cl) Thin Films Analysed by: In Situ X-Ray Diffraction. *J. Mater. Chem. A* **2018**, *6* (24), 11496–11506. https://doi.org/10.1039/c8ta02775g.

(44) Baikie, T.; Fang, Y. N.; Kadro, J. M.; Schreyer, M.; Wei, F. X.; Mhaisalkar, S. G.; Graetzel, M.; White, T. J. Synthesis and Crystal Chemistry of the Hybrid Perovskite (CH3NH3) PbI3 for Solid-State Sensitised Solar Cell Applications. *J. Mater. Chem. A* **2013**, *1* (18), 5628–5641. https://doi.org/10.1039/c3ta10518k.

(45) Singh, S.; Li, C.; Panzer, F.; Narasimhan, K. L.; Graeser, A.; Gujar, T. P.; Köhler, A.; Thelakkat, M.; Huettner, S.; Kabra, D. Effect of Thermal and Structural Disorder on the Electronic Structure of Hybrid Perovskite Semiconductor CH3NH3PbI3. *J. Phys. Chem. Lett.* **2016**, *7* (15), 3014–

3021. https://doi.org/10.1021/acs.jpclett.6b01207.

(46) Song, Z.; Watthage, S. C.; Phillips, A. B.; Tompkins, B. L.; Ellingson, R. J.; Heben, M. J. Impact of Processing Temperature and Composition on the Formation of Methylammonium Lead Iodide Perovskites. *Chem. Mater.* **2015**, *27* (13), 4612–4619. https://doi.org/10.1021/acs.chemmater.5b01017.

(47) Yi Yang; Fei Gao; Shiwu Gao; Su-Huai Wei. Origin of the Stability of Two-Dimensional Perovskites: A First-Principles Study. *J. Mater. Chem. A* **2018**, *6* (30), 14949–14955. https://doi.org/10.1039/C8TA01496E.

(48) Jacobsson, T. J.; Correa-Baena, J.-P.; Anaraki, E. H.; Philippe, B.; Stranks, S. D.; Bouduban, M. E. F.; Tress, W.; Schenk, K.; Joë L Teuscher, ⊗; Moser, J.-E.; Hå Kan Rensmo, ¶; Hagfeldt, A. Unreacted PbI 2 as a Double-Edged Sword for Enhancing the Performance of Perovskite Solar Cells. **2016**. https://doi.org/10.1021/jacs.6b06320.

(49) Philippe, B.; Saliba, M.; Correa-Baena, J. P.; Cappel, U. B.; Turren-Cruz, S. H.; Grätzel, M.; Hagfeldt, A.; Rensmo, H. Chemical Distribution of Multiple Cation (Rb+, Cs+, MA+, and FA+) Perovskite Materials by Photoelectron Spectroscopy. *Chem. Mater.* **2017**, *29* (8), 3589–3596. https://doi.org/10.1021/acs.chemmater.7b00126.

(50) Roß, M.; Gil-Escrig, L.; Al-Ashouri, A.; Tockhorn, P.; Jošt, M.; Rech, B.; Albrecht, S. Co-Evaporated p-i-n Perovskite Solar Cells beyond 20% Efficiency: Impact of Substrate Temperature and Hole-Transport Layer. *ACS Appl. Mater. Interfaces* **2020**, *12* (35), 39261–39272. https://doi.org/10.1021/acsami.0c10898.

(51) Sun, S.; Buonassisi, T.; Correa-Baena, J. P. State-of-the-Art Electron-Selective Contacts in Perovskite Solar Cells. *Adv. Mater. Interfaces* **2018**, *5* (22).

https://doi.org/10.1002/ADMI.201800408.

(52) Castro-Méndez, A. F.; Hidalgo, J.; Correa-Baena, J. P. The Role of Grain Boundaries in Perovskite Solar Cells. *Advanced Energy Materials*. Wiley-VCH Verlag October 1, 2019, p 1901489. https://doi.org/10.1002/aenm.201901489.

**Table of content image**